DOI: 10.61782/fa.2025.0920

FORUM ACUSTICUM EURONOISE 2025

TUNABLE MICROPERFORATED PANEL ACOUSTIC ABSORBERS WITH COUPLING EFFECTS UNDER GRAZING FLOW

Ying Li[1] **and Yat Sze Choy**[1*]
[1] Department of Mechanical Engineering, The Hong Kong Polytechnic University, Hong Kong Special Administrative Region, People's Republic of China

ABSTRACT

Design for highly effective acoustic meta-liners with broadband sound attenuation under grazing flow is challenging due to performance degradation with high flow speeds and intricate internal structures involved. In this study, a tunable microperforated panel (MPP) acoustic absorber is proposed that leverages the coupling effects between its sub-components to achieve broadband sound absorption across static and flow conditions. A theoretical framework combining acoustic radiation theory with modal superposition principles is developed to predict the performance of the proposed absorber. The theoretical and numerical analysis clarifies how coupling effects enhance the absorption troughs in the proposed absorber. Finally, a broadband acoustic liner, composed of multiple optimized coupled MPP absorbers is proposed. Experimental investigations validate the sound absorption performance of the proposed acoustic liner under grazing flow, highlighting the potential of our theoretical model and coupled MPP absorbers to advance acoustic meta-liner design.

Keywords: *Flow and acoustic interactions, microperforated panel absorber; two-dimensional theoretical model; broadband sound absorption.*

1. INTRODUCTION

The highly effective broadband absorption of low-frequency sound is a growing and challenging topic for acoustic liners in aero-engines and ventilation ductwork systems [1]. Traditional porous materials and microperforated panels (MPPs) absorbers require sufficient thickness compared with the wavelength to control low-frequency sound, which hinders their wide application in practice. In recent years, acoustic metamaterials (AMMs) [2] that are artificial periodic structures with subwavelength building blocks provide a new idea for the design of low-frequency sound absorbers. A number of functionalities and applications have been proved and achieved based on AMMs. To enhance the sound absorption bandwidth, many metamaterial designs spatially stack resonators with varying cavity depths to connect all resonance frequency peaks. This approach, however, necessitates a surprisingly large number of units to effectively suppress noise. Inadequate numbers of resonant elements lead to unsatisfied absorption in the troughs, thereby limiting the applicability of AMMs in duct systems and room acoustics.

Building on these foundational principles and strategies, current advancements in AMM technology have led to their application in developing effective acoustic liners under flow conditions. However, increasing flow speeds trigger stronger coupling between grazing flows and acoustic waves, resulting in substantial degradation of meta-liner absorption performance [3-5]. To date, few metaliner designs have fully achieved simultaneous broadband noise reduction and stable absorption efficacy across varying flow velocities, representing a critical barrier to practical applications.

In this study, a coupled acoustic absorber (CAA) featuring inserted MPPs and shared cavities is proposed to achieve broadband sound absorption across static and flow conditions. The objectives of this study are as follows: (1) To propose a two-dimensional (2D) model for predicting the acoustic performance of the CAA based on sound radiation theory in a rigid-walled duct. (2) To design a coupled MPP absorbers that achieves broadband noise

[*] ***Corresponding author***: *mmyschoy@polyu.edu.hk.*

reduction while preserving effective broadband sound absorption performance under increasing flow velocities

2. THEORETICAL MODELLING

The proposed CAA comprised inserted MPPs and shared cavities, as shown in Fig. 1. The solid line denotes the rigid wall while the dashed line is the MPP in the TAA. The shaded region denotes the acoustically rigid block. We assumed that a normally incident wave p_{inc} impinged on the surface of the CAA. The acoustic pressure outside of the cavity is $p_{\text{a}} = 2p_{\text{inc}} + p_{\text{rad\_duct}}$, where $p_{\text{rad\_duct}}$ denotes the pressure radiating from the surface. As shown in Fig. 1, the n-th MPP is located at surface $S_{\text{p\_n}}$ with a length of L_{n}. The particle velocity over the MPP surface $S_{\text{p\_n}}$ is expanded as a series of sine functions as

$$v_{\text{p\_n}}(x) = \sum_{q=1}^{\text{Q}} V_{\text{p\_n,q}} \phi_{\text{p\_n,q}}(x), \tag{1}$$

with

$$\phi_{\text{p\_n,q}}(x) = \sin\left(\frac{q\pi}{L_{\text{n}}} x\right) \tag{2}$$

where $V_{\text{p\_n,q}}$ and $\varphi_{\text{p\_n,q}}$ are the q-th modal amplitude and modal shape of the n-th MPP, respectively. q is the modal indices. With the proper truncation of the decomposition series, Eq. (1) can accurately represent the averaged particle velocity fields $v_{\text{p\_n}}$ except at the boundary edges. Subsequently, the pressure field in the duct above the meta-surface can be formally expressed as a superposition of plane wave modes [6]

$$p_{\text{rad\_duct}}(x,0) = \rho_0 \sum_{g=0}^{\text{G}} \frac{\omega \psi_{\text{d,g}}(x)}{W \kappa_{\text{d,g}}} \int_{S_{\text{p\_1}}} \psi_{\text{d,g}}(x') v_{\text{p\_1}}(x') ds' \tag{3}$$

where, $\psi_{\text{d,g}}(x)$ is the g-th cross-sectional mode shape function of the duct, $\kappa_{\text{d,g}}$ is the propagation constant along the duct given by $-i\sqrt{k_{\text{d,g}}^2 - \left(k - i\alpha_{\text{duct}}\right)^2}$, $k_{\text{d,g}}$ is the cross-sectional characteristic propagation constant, and k is the propagation constant without absorption. α_{duct} is the absorption coefficient of the duct defined in [7]. $\psi_{\text{d,g}}(x) = \sqrt{2 - \delta_{0,\text{g}}} \cos\left(g\pi x / W\right)$ and $k_{\text{d,g}}^2 = \left(g\pi / W\right)^2$. $\delta_{0,g}$ is the Kronecker delta function, which is equal to zero when $g \neq 0$ and unity when $g = 0$. ρ_0 is the density of air and ω is the radial frequency. g is the modal index.

On the other hand, the acoustic pressure inside n-th channel excited by the velocity distribution on the adjacent r-th MPP ($r = n$ or n+1) can be separated into two parts: the sound radiated from the velocity distribution on the r-th MPP, and the corresponding reflected wave by the boundaries of the channel walls as $p_{\text{MPP\_r}}^{\text{ch\_n}} = p_{\text{rad\_r}}^{\text{ch\_n}} + p_{\text{ref\_r}}^{\text{ch\_n}}$. According to Doak's theory [6], the sound pressure radiated by a sound source distribution in r-th MPP in the n-th channel can be expressed as

$$p_{\text{rad\_r}}^{\text{ch\_n}}(x,y) = \rho_0 \sum_{m=0}^{\text{M}} \frac{\omega \psi_{\text{n,m}}(y)}{2D_{\text{n}} \kappa_{\text{n,m}}} \int_{S_{\text{p\_r}}} \left[H(x - x') e^{-i\kappa_{\text{n,m}}(x-x')} + H(x' - x) e^{i\kappa_{\text{n,m}}(x-x')} \right] \psi_{\text{n,m}}(D_*) v_{\text{p\_r}}(x') ds', \tag{4}$$

where H denotes the Heaviside function. $\psi_{\text{n,m}}(y)$ is the cross-section mode shape functions of the n-th channel, and $\kappa_{\text{n,m}}$ is the propagation constant along the n-th channel axis given by $-i\sqrt{k_{\text{n,m}}^2 - \left(k - i\alpha_{\text{n,wall}}\right)^2}$, where $k_{\text{n,m}}$ is the cross-sectional characteristic propagation constant. $\alpha_{\text{n,wall}}$ is the absorption coefficient of the n-th channel, defined in ref [7]. $\psi_{\text{n,m}}(y) = \sqrt{2 - \delta_{0,\text{m}}} \cos\left(m\pi y / D_{\text{n}}\right)$ and $k_{\text{n,m}}^2 = \left(m\pi / D_{\text{n}}\right)^2$. m is the modal index. $D_* = -D_{\text{n}}$ ($n < q$) or 0 ($n = q$).

The reflected wave induced by a sound source distribution in r-th MPP in the n-th channel is calculated in a manner similar to the radiation pressure in Eq. (4), except that the Heaviside functions are replaced by the unknown coefficients $C_{\text{n,m}}^{+}$ and $C_{\text{n,m}}^{-}$ as $C_{\text{n,m}}^{+} = \frac{e^{ik_{\text{n,m}}(2W - 2x')} + 1}{e^{ik_{\text{n,m}}(2W)} - 1}$ and $C_{\text{n,m}}^{-} = \frac{e^{ik_{\text{n,m}}(2W + 2x')} + 1}{e^{ik_{\text{n,m}}(2W)} - 1}$, respectively.

2.1 Pressure gradient at the MPP

The acoustic boundary condition of the MPP mounted on the upper surface $S_{\text{p\_1}}$ can be described as

$$Z_{\text{MPP\_1}} v_{\text{p\_1}}(x,0) = \frac{1}{\rho_0 c_0} \left[p_{\text{MPP\_1}}^{\text{ch\_1}}(x,0) + p_{\text{MPP\_2}}^{\text{ch\_1}}(x,0) - 2p_{\text{inc}} - p_{\text{rad\_duct}}(x,0) \right] \tag{5}$$

where c_0 is the sound speed of air. Substituting Eqs. (1-4) into Eq. (5), and meanwhile multiplying $\phi_{\text{p\_1,q'}}(x)$ on both sides to apply the orthogonal property, and integrating over the MPP yields

$$(\boldsymbol{A}^{\mathrm{sur}}+\boldsymbol{A}^{\mathrm{radMPP\_1}}+\boldsymbol{A}^{\mathrm{rad\_11}}+\boldsymbol{A}^{\mathrm{ref\_11}})\boldsymbol{V}_{\mathrm{p\_1}} +(\boldsymbol{A}^{\mathrm{rad\_12}}+\boldsymbol{A}^{\mathrm{ref\_12}})\boldsymbol{V}_{\mathrm{p\_2}}=\boldsymbol{A}^{\mathrm{inc}} \quad (6)$$

where $\boldsymbol{A}^{*}$ is the Q × Q matrix, and the $\boldsymbol{V}_{*}$ is the Q × 1 matrix. The acoustic impedance of the *n*-th MPP is determined using the acoustic impedance model (without flow) proposed by Maa [8]:

$$Z_{\mathrm{MPP\_n}}=\frac{32\mu t_{\mathrm{MPP\_n}}}{\sigma_{\mathrm{MPP\_n}}d_{\mathrm{MPP\_n}}^{2}}\left[\left(1+\frac{(K_{\mathrm{n}})^{2}}{32}\right)^{\frac{1}{2}}+\frac{\sqrt{2}}{8}K_{\mathrm{n}}\frac{d_{\mathrm{MPP\_n}}}{t_{\mathrm{MPP\_n}}}\right], +\mathrm{i}\frac{\rho_0\omega t_{\mathrm{MPP\_n}}}{\sigma_{\mathrm{MPP\_n}}}\left[1+\left(9+\frac{(K_{\mathrm{n}})^{2}}{2}\right)^{-1/2}+0.85\frac{d_{\mathrm{MPP\_n}}}{t_{\mathrm{MPP\_n}}}\right] \quad (7)$$

where $d_{\mathrm{MPP\_n}}$, $t_{\mathrm{MPP\_n}}$, and $\sigma_{\mathrm{MPP\_n}}$ are the diameter, thickness, and porosity of the *n*-th MPP, respectively. μ are the density and viscosity of air. $K_{\mathrm{n}}=(d_{\mathrm{MPP\_n}}/2)\sqrt{\rho_0\omega/\mu}$ is a parameter describing the ratio of the radius to the viscous boundary layer thickness inside the hole.

Analogously, by reorienting the reference axis to the left-hand side of the N-th (last) channel, the acoustic boundary condition on the MPP mounted at the surface $S_{\mathrm{p\_n}}$ can be described as

$$Z_{\mathrm{MPP\_n}}v_{\mathrm{p\_n}}(x,0)=\frac{1}{\rho_0 c_0}\left[p_{\mathrm{MPP\_n}}^{\mathrm{ch\_n}}(x,0)-p_{\mathrm{MPP\_n}}^{\mathrm{ch\_n\text{-}1}}(x,0)-p_{\mathrm{MPP\_n\text{-}1}}^{\mathrm{ch\_n\text{-}1}}(x,0)\right]. \quad (8)$$

Substituting Eqs. (1-4) into Eq. (8), multiplying $\phi_{\mathrm{p\_n,q}}(x)$ on both sides and integrating over the MPP yields

$$(\boldsymbol{A}^{\mathrm{rad\_(N)(N\text{-}1)}}+\boldsymbol{A}^{\mathrm{ref\_(N)(N\text{-}1)}})\boldsymbol{V}_{\mathrm{p\_N\text{-}1}}+(\boldsymbol{A}^{\mathrm{radMPP\_N}}+\boldsymbol{A}^{\mathrm{rad\_NN}} +\boldsymbol{A}^{\mathrm{ref\_NN}}+\boldsymbol{A}^{\mathrm{up\_rad\_NN}}+\boldsymbol{A}^{\mathrm{up\_ref\_NN}})\boldsymbol{V}_{\mathrm{p\_N}}=\boldsymbol{0}, \quad (9)$$

where $\boldsymbol{A}^{*}$ is the Q × Q matrix, and the $\boldsymbol{V}_{*}$ is the Q × 1 matrix.

2.2 System matrix

Based on Eq. (8) and Eq. (9), the first and last row of the systematic matrix equation, considering the coupling of layers in CAA yields

$$\left[\boldsymbol{A}^{\mathrm{sur}}+\boldsymbol{A}^{\mathrm{radMPP\_1}}+\boldsymbol{A}^{\mathrm{rad\_11}}+\boldsymbol{A}^{\mathrm{ref\_11}}\quad \boldsymbol{A}^{\mathrm{rad\_12}}+\boldsymbol{A}^{\mathrm{ref\_12}}\quad \cdots\quad \boldsymbol{0}\right]\left[\boldsymbol{V}_{\mathrm{p\_1}}\right]=\left[\boldsymbol{A}^{\mathrm{inc}}\right], \quad (10)$$

and

$$\left[\boldsymbol{0}\quad \cdots\quad \boldsymbol{A}^{\mathrm{rad\_(N)(N\text{-}1)}}+\boldsymbol{A}^{\mathrm{ref\_(N)(N\text{-}1)}}\quad \boldsymbol{A}^{\mathrm{radMPP\_N}}+\boldsymbol{A}^{\mathrm{rad\_NN}}+\boldsymbol{A}^{\mathrm{ref\_NN}}+\boldsymbol{A}^{\mathrm{up\_rad\_NN}}+\boldsymbol{A}^{\mathrm{up\_ref\_NN}}\right]\left[\boldsymbol{V}_{\mathrm{p\_N}}\right]=\left[\boldsymbol{0}\right], \quad (11)$$

respectively.

Under a similar derivation, an equation that describes the *n*-th MPP (n = 2,3···N-1) of the CAA can be expressed as follows

$$(\boldsymbol{A}^{\mathrm{rad\_(n)(n\text{-}1)}}+\boldsymbol{A}^{\mathrm{ref\_(n)(n\text{-}1)}})\boldsymbol{V}_{\mathrm{p\_n\text{-}1}}+(\boldsymbol{A}^{\mathrm{radMPP\_n}}+\boldsymbol{A}^{\mathrm{rad\_nn}}+\boldsymbol{A}^{\mathrm{ref\_nn}} +\boldsymbol{A}^{\mathrm{up\_rad\_nn}}+\boldsymbol{A}^{\mathrm{up\_ref\_nn}})\boldsymbol{V}_{\mathrm{p\_n}}+(\boldsymbol{A}^{\mathrm{rad\_n(n+1)}}+\boldsymbol{A}^{\mathrm{ref\_n(n+1)}})\boldsymbol{V}_{\mathrm{p\_n+1}}=\boldsymbol{0}. \quad (12)$$

A more generalized systematic matrix for calculating the N-layer CAA is constructed by incorporating Eqs. (10-12). Any remaining entries in this generalized systematic matrix should be filled with zero matrices. For the sake of conciseness, the complete formulation of the generalized systematic matrix for the N-layer CAA is omitted here.

The unknown coefficient $\boldsymbol{V}_{\mathrm{p\_n}}$ can be obtained after solving the generalized systematic matrix for the N-layer CAA. Thus, the sound pressures inside the duct and structure can be calculated. After obtaining the sound pressure field, the absorption coefficient of the CAA is calculated as follows [9]:

$$a=\frac{\rho_0 c_0\int_{S_{\mathrm{p\_1}}}\mathrm{Re}\left(p_{\mathrm{a}}\cdot v_{\mathrm{p\_1}}^{*}\right)ds}{W}, \quad (13)$$

where the asterisk denotes the complex conjugate.

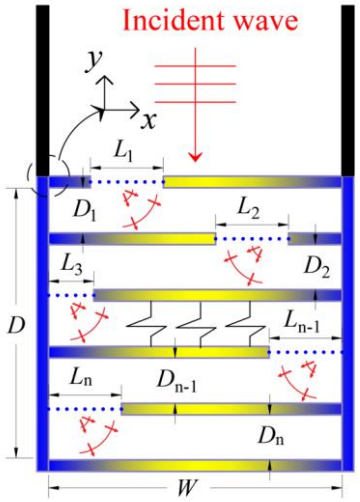

Figure 1. Two-dimensional schematic diagram of the CAA for theoretical modelling.

3. RESULTS AND DISCUSSION

To validate the proposed 2D theoretical model, the commercial software COMSOL Multiphysics and the finite element method (FEM) were used to calculate the absorption coefficients of the CAA. The predicted absorption coefficients for the two-layer coupled CAA are illustrated in. Fig. 2. The following structural parameters of the CAA were used: $W_1 = W_2 = 50$ mm, $D_1 = D_2 = 20$ mm. The diameter, thickness and porosity of the surface MPP are 1 mm, 1 mm, and 0.015. The diameter, thickness and porosity of the interior MPP are 0.15 mm, 1 mm, and

0.0123. As shown in Fig. 2, for the two-layer CAA calculated via the FEM, a near-total absorption peak appears at 600 Hz. The second peak occurs at 980 Hz. The outcome obtained by the proposed 2D model (solid line) is in good agreement with that calculated by the FEM (rhombus) for the two-layer CAA, both in terms of peak frequency and peak value. This demonstrates that the proposed 2D model accurately predicts the acoustic performance of CAA. The first peak is generated by the resonance of the right sub-resonator (star), while the second peak originates from the left sub-resonator (circle). Notably, a pronounced dip occurs at 780 Hz with an absorption value of approximately 0.86. This represents a significant enhancement compared to the case without the interior MPP (square), where the dip value is only 0.48.

To further investigate the enhancement mechanism induced by coupling effects, Fig. 3 presents the sound pressure and velocity distributions within the two-layer CAA at the first peak, dip, and second peak frequencies. As shown by the white arrows, at the dip frequency, a high acoustic velocity passes through the interior MPP, accompanied by high acoustic pressure in both left and right sub-resonators. This suggests that the superior sound absorption performance at the dip frequency arises from the synergistic effects of all MPPs. In contrast, at the peak frequencies, although only one sub-resonator dominates, the partial acoustic velocity through the interior MPP still contributes to a minor enhancement of the peak absorption value.

To further investigate the sound absorption mechanism and the role of the inserted MPPs in the proposed CAA, we conducted a modal analysis. Fig. 4 presents the modal amplitude ($|V_p|$) of particle velocity across each MPP interface in the two-layer CAA, as calculated by our theoretical model, focusing on the first peak (600 Hz), trough (780 Hz), and second peak (980 Hz). At the peak frequencies (Figs. 4a and 4c), while the dominant acoustic velocity occurs at the surface MPP, a non-negligible acoustic flow through the interior MPP is also observed, which can be absorbed by the interior MPP. In contrast, at the dip frequency (Fig. 4b), all MPPs exhibit significant acoustic velocity, further confirming that the enhanced sound absorption at this dip frequency stems from the collective contribution of all MPPs.

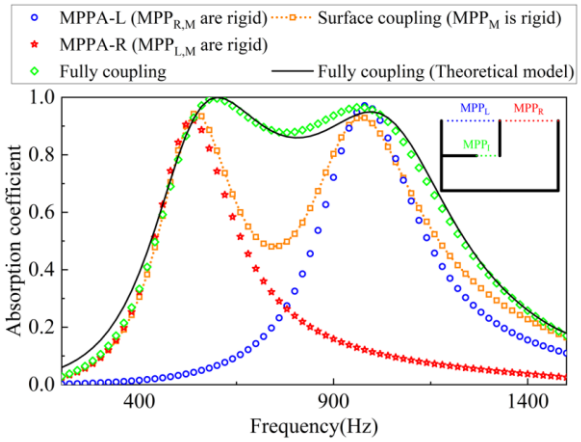

Figure 2. The predicted absorption coefficients for the two-layer CAA.

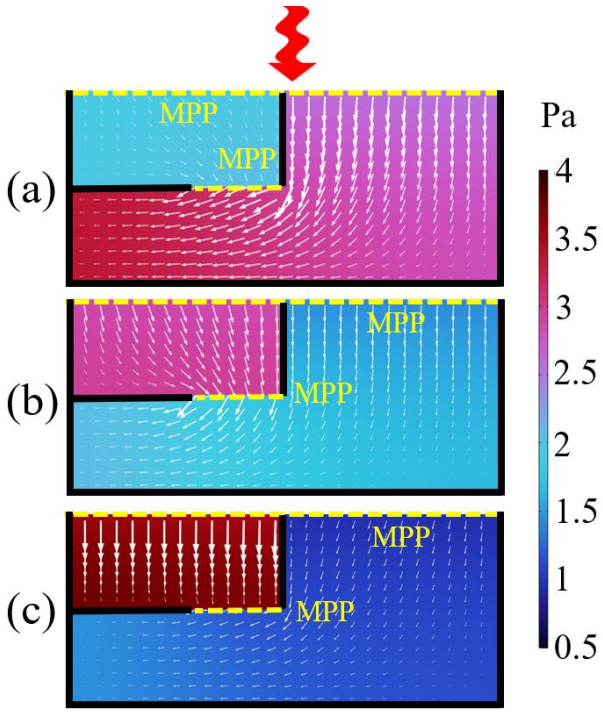

Figure 3. Distribution of sound pressure and velocity (arrow) at (a) 600 Hz, (b) 780 Hz and (c) 980 Hz. The direction of arrows denotes the intensity flow direction, and the size represents the velocity magnitude.

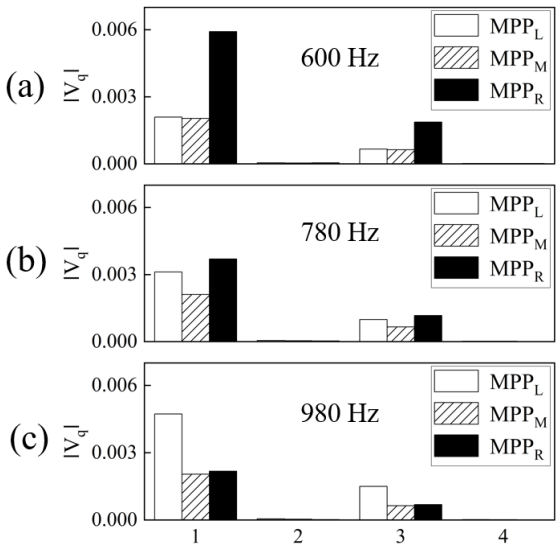

Figure 4. Modal amplitude of particle velocity over the MPP interface in the 2-layer CAA at (a) the first peak, (b) trough, and (c) second peak frequencies.

4. FLOW EFFECT ON THE CAA

Numerous efforts have been made to establish prediction formulas for the acoustic properties of orifices under various flow conditions. However, they have different assumptions for flow characteristics or do not consider the influence of shallow cavities behind the holes; thus, these formulae may forecast discrepant acoustic properties towards an orifice. To better understand the fluid dynamics when the flow passes over the proposed CAA, the flow patterns of the MPP (d = 1 mm) and four backed cavities with different cavity depths (2 mm and 6 mm) under grazing flow speeds of 34 m/s were investigated using the CFD method. In this study, the Reynolds averaged Navier–Stokes (RANS) simulations were applied to find the statistical average of the turbulent flow, and the shear stress transport (SST) k–ω turbulence model was utilized to account for the effects of turbulence on this averaged flow. The geometry of the computational model is shown in Fig. 5(a). The orifices and accompanying cavity were located on the underside of the duct. The cross-section of the main duct was 24 mm × 24 mm. The length of the upstream duct was set to 1000 mm, to generate a fully developed turbulent boundary layer in front of the orifice. The distance between the tested orifice and outlet (300 mm) was more than 50 times the orifice diameter. This ensured that any vorticity could be dissipated along this distance. The inlet of the duct was set as the mass-flow inlet boundary condition. A pressure-outlet boundary condition was imposed upon the duct outlet at standard atmospheric pressure (1 atm). The non-reflection boundary condition (NRBC) was applied to the inlet and outlet. The remaining walls of the main duct, orifice, and cavities were set as stationary and adiabatic walls, without any slip. Fig. 5(b) illustrates the vorticity distribution across the resonator surface. The consistent vorticity patterns observed at each surface orifice demonstrate that even under moderately high flow speeds (34 m/s), the hole spacing is sufficient to minimize inter-hole coupling effects. Notably, in the shallow-cavity configuration (left resonator), the injected flow through the surface MPP impinges on the second-layer MPP, effectively modulating its acoustic impedance through a mechanism analogous to bias flow. Conversely, in the deep-cavity configuration (right resonator), the injected flow dissipates before reaching the second MPP, thereby eliminating this interference.

Based on these observations for the absence of inter-hole coupling and backing cavity depths exceeding 10 mm, we adopt the flow-dependent MPP impedance model proposed by Li and Choy [10] in Eq. (9) to predict the acoustic liner's acoustic performance under grazing flow (Section 5).

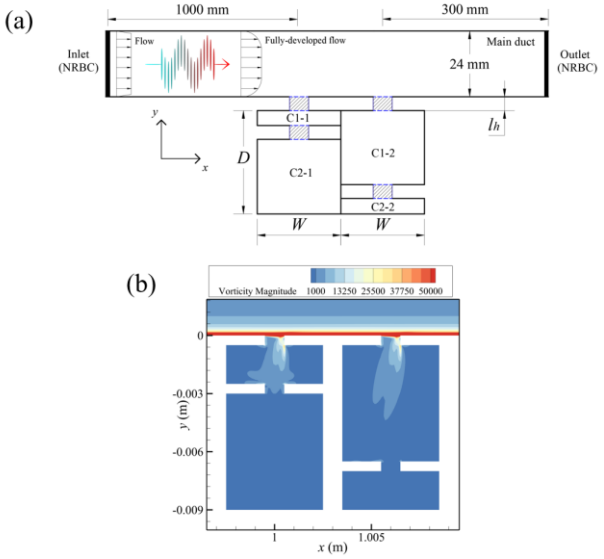

Figure 5. (a) Geometry of the computational model and (b) vorticity distribution.

5. EXPERIMENTAL INVESTIGATION

To test the sound absorption performance of the proposed acoustic liner and validate the proposed theoretical and numerical models under grazing flow, *TL* measurements of the acoustic liner consisting of four CAA were performed. Each CAA contains four layers. The following structural parameters of each CAA were used: $W = 100$ mm, $D_1 = D_2 = D_3 = D_4 = 20$ mm. The diameter, thickness and porosity of the surface MPP are 0.3 mm, 0.5 mm, and 0.022. The diameter, thickness and porosity of the interior MPPs are 0.5 mm, 0.5 mm, and 0.02. A photography of the test rig and tested acoustic liner are shown in Fig. 6(a). The experiment was conducted in a quiet mini-wind tunnel using a working section of dimensions 100 mm × 100 mm (cross-section) and 1.8 m (length). The first cut-on frequency of the duct was 1700 Hz, and the turbulence intensity of the fully developed grazing flow in the upstream sections was below 0.1%. The MPPs of the acoustic liner were fabricated from stainless steel via etching. Other components of the acoustic liner were 3D-printed. Two proposed acoustic liners were mounted on the two sides of the test section of the duct. Two pairs of B&K 1/2 in. condenser microphones (type no. 4187) were installed up- and down-stream of the tested absorber. The installments of four microphones are shown in Fig. 6(a) via the labels M1–4. The travelling wave components in the duct could be resolved by each pair of microphones. Using the approach of two independent sound sources at two positions to simulate physical anechoic termination, the *TL* of the acoustic liner was determined. The measured and predicted TL are present in Fig. 6(b). In general, the experimental results agree well with the predicted TL in terms of the tendency, under different flow speeds. Some discrepancy in peak values between experiments and prediction mainly results from the fabrication error of the 3D-printed model. As demonstrated in Fig. 6(b), the proposed acoustic liner achieves an average transmission loss of 18.92 dB across the 200-1700 Hz frequency range under static conditions (denoted by circles). When the flow speed increases to 25 m/s, the liner maintains an average transmission loss of 17.89 dB over the same bandwidth (square), representing only a 5.7% performance reduction. These experimental findings confirm that by localizing acoustic energy dissipation within embedded MPPs, the CAA significantly suppresses performance degradation caused by grazing-flow-induced aeroacoustic coupling. Our results provide new insights into the design of metamaterials for aero-noise control engineering and may promote the development of meta-liners for airflow applications.

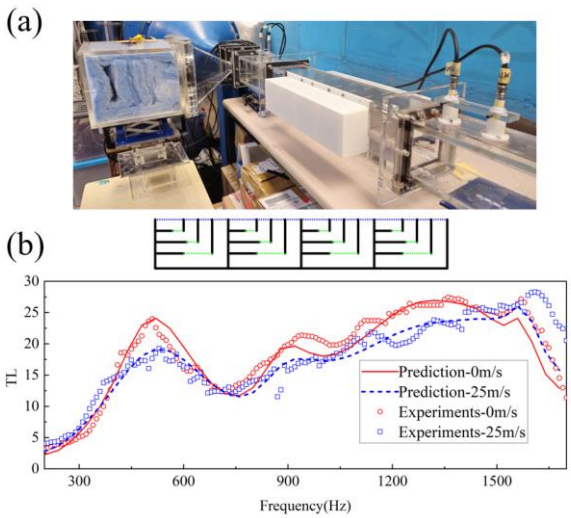

Figure 6. (a) photography of the test rig and tested acoustic liner and (c) TL obtained by prediction and experiments.

6. CONCLUSION

A coupled acoustic absorber (CAA) comprised inserted MPPs and shared cavities was proposed with broadband sound reduction under grazing flow. A two-dimensional model for predicting the acoustic performance of the CAA was proposed based on sound radiation theory in a rigid-walled duct. The sound absorption characteristics of the CAA was investigated via theoretical model and numerical model (finite element method). Consistent predicted results from both models manifested that the 2D theoretical model can accurately predict the acoustic performance of the CAA. In addition, the theoretical and numerical results revealed that the enhancement of the CAA's absorption troughs arises from the synergistic effects of all MPPs. Finally, experimental investigation was conducted and revealed that by localizing acoustic energy dissipation within embedded MPPs, the CAA significantly suppresses performance degradation caused by grazing-flow-induced aeroacoustic coupling. Our results provide new insights into the design of metamaterials for aero-noise control engineering and may promote the development of meta-liners for airflow applications.

7. ACKNOWLEDGMENTS

The authors would like to acknowledge the funding from The Hong Kong Polytechnic University and the Research Grants Council of the Hong Kong SAR (PolyU 15207221).

8. REFERENCES

[1] C. Lahiri, F. Bake, "A review of bias flow liners for acoustic damping in gas turbine combustors," *J. Sound Vib.*, 400 (2017) 564-605.

[2] Z. Liu, X. Zhang, Y. Mao, Y. Zhu, Z. Yang, C.T. Chan, P. Sheng, "Locally resonant sonic materials," *Science*, 289 (2000) 1734-1736.

[3] X. Zhang, L. Cheng, "Acoustic silencing in a flow duct with micro-perforated panel liners," *Appl. Acoust.*, 167 (2020) 107382.

[4] S. Huang, E. Zhou, Z. Huang, P. Lei, Z. Zhou, Y. Li, "Broadband sound attenuation by meta-liner under grazing flow," *Appl. Phys.* Lett., 118 (2021).

[5] J. Zhao, F. Wu, Z.-G. Ju, M. Hu, X. Zhang, D. Li, S.-L. Yan, K.-L. Liu, "Neck-embedded acoustic meta-liner for the broadband sound-absorbing under the grazing flow with a wide speed range," *J. Phys. D: Appl. Phys.*, 56 (2022) 045401.

[6] P. Doak, "Excitation, transmission and radiation of sound from source distributions in hard-walled ducts of finite length (I): The effects of duct cross-section geometry and source distribution space-time pattern," *J. Sound Vib.*, 31 (1973) 1-72.

[7] G. Yu, L. Cheng, D. Li, "A three-dimensional model for T-shaped acoustic resonators with sound absorption materials," *J. Acoust. Soc. Am.*, 129 (2011) 3000-3010.

[8] D.-Y. Maa, "Theory and design of microperforated panel sound-absorbing constructions," *Sci. Sin.*, 18 (1975) 55-71.

[9] W. Yang, Y. Choy, Y. Li, "Acoustical performance of a wavy micro-perforated panel absorber," *Mech. Syst. Signal Proc.*, 185 (2023) 109766.

[10] Y. Li, Y.S. Choy, "Acoustic behaviour of micro-perforated panel backed by shallow cavity under fully developed grazing flow," *J. Sound Vib.*, 569 (2024) 117985.